Journal of Renewable Energies 28 (2025) 207 – 221

DOI: https://doi.org/10.54966/jreen.v28i1.1370

Journal of Renewable Energies

Revue des Energies Renouvelables

Journal home page: https://revue.cder.dz/index.php/rer

Research paper

The vertical architecture of parallel flow field high temperatures proton exchange membrane fuel cell and its effects on the consumption of reactants and products

Youcef Aouabdia [a], **Mouloud Laidoudi** [a,*], **Nawel Outili** [b]

[a] *Département de Physique & Chimie, Ecole Normale Supérieure Assia Djebar, Constantine, Algeria*

[b] *Faculty of Process Engineering, University of Constantine 3, Saleh Boubnider, Algeria*

ARTICLE INFO

Article history:
Received February 20 , 2025
Accepted June 25, 2025
Available online June 25, 2025
Published June 26, 2025

Keywords:
Fast consumption of reactant,
Multi- channels,
HT- PEMFCs in series,
Better reactant distribution,
Polybenzimidazole,
Performance.

ABSTRACT

In this paper, we investigate the efficiency and, to minimize the size of high-temperature polymer electrolyte membrane fuel cells (HT-PEMFC), the consumption and distribution of reactants O2 and H2 in channels, as well as the products of a vertical architecture instead of the horizontal architecture. Moreover, we compare our numerical simulation results to experimental results of other researchers. In addition, we consider in this work a polybenzimidazole membrane doped with phosphoric acid, with four types of parallel flow field stack cells. A single cell consists of seven sub-parts, a double cell consists of thirteen sub-parts, a triple cell consists of nineteen sub-parts, and a four-cell consists of twenty-five sub-parts. 3D model, single phase, ideal gases, incompressible gases, impermeable membrane for the reactant gases and water, laminar flow, steady state, and isothermal model were taken into consideration in our study. For the reason to check the efficiency, we investigate the polarization curves (V-I) for this target. To check the distribution of reactants in the channels and the size decrease of the cells, we study hydrogen, oxygen, and water distribution patterns.

1. INTRODUCTION

Among the issues raised in laboratories in all over the world are either to find a new effective source of energy or to develop the known sources of energy. Among the well-known up-to-date sources of energy are nuclear energy, combustion engines based on fossil fuels, and solar cells energy, fans wind energy, fuel cells, water wave energy, biomass energy, and hydroelectric energy. Based on the kind of membrane, fuel cells are classified as follows: 1) Alkaline fuel cells (AFC) with a membrane of aqueous

---

* *Corresponding author, E-mail address: laidoudi.mouloud@ensc.dz*
Tel :+ 213 664759048

ISSN: 1112-2242 / EISSN: 2716-8247

solution of potassium hydroxide operate at 50-200°C. 2) Solid oxide fuel cells (SOFC) with a membrane of ceramics operate at 600-1000°C. 3) Molten carbonate fuel cells (MCFC) with a membrane of a solution of lithium, sodium, and potassium carbonates operate at 600-1000°C. 4) Phosphoric acid fuel cells (PAFC) with a membrane of phosphoric acid solution operate at 175-200°C. 5) Direct methanol fuel cells (DMFC) with a membrane of perfluorosulfonic acid operate at 50-100°C. 6) Direct borohydride fuel cells (DBFC) with anion and cation exchange membranes which operate at 50-100°C. 7) Proton exchange membrane fuel cells (PEMFC) with a membrane of perfluorosulfonic acid "Nafion" operate at 50-100°C and 8) High-temperature polymer electrolyte membrane fuel cell (HT-PEMFC) with a membrane of polybenzimidazole (PBI) and operates at 120-200°C (Caglagan et al. (2018).

Regarding fuel cells based on polymer membranes, so far there are two kinds: a) PEMFC based on Nafion membranes, which operates at temperatures ranging from 50°C up to 100 °C; they call it low-temperature PEMFC (LT-PEMFC). Among its characteristics, the water produced at its cathode catalyst layer (C-CL) will be in the form of liquid, as result a streaming of water appears in the cathode electrode during the operation, leading to decay of produced current, so it needs a sophisticated water management appliances and low tolerance for CO poisoning (Wu et al., 2016). In addition, this type of cell needs humidification of reactant gases during the operation to prevent dehydration of the Nafion membrane. b) The second kind is HT-PEMFC based on PBI membrane, which operates at a temperature range of 120-200 °C. The HT-PEMFC does not need the humidification of reactant gases during the operation (Xia et al., 2018). Also, at 150°C, the CO tolerance of HT-PEMFC is so much higher than the CO tolerance of LT-PEMFC (Qingfeng Li et al., 2003).

Water produced in the C-CL of HT-PEMFC will be in the form of vapor only; therefore, it is a single-phase system. Hence, the increasing of operating temperatures of HT-PEMFC sorted out many problems, such as 1) No more streaming water in the C-CL. 2) Increases kinetic reaction rate leading to improved performance (Cheddie & Munroe, 2006), and 3) decreases the cell ohmic resistance (Peng & Lee, 2006). The advantages of PBI membrane are that it does not need humidification during the operation of HT-PEMFC, has strong mechanical property, at high temperatures has a sufficient thermal and mechanical stability, and has a water tow coefficient of almost zero. The protonic conductivity of PBI is related to 1) the amount "concentration" and the kind of acid doping, 2) the temperature, and 3) the synthesis method. So far, the highest value of ionic conductivity of BPI is 13 S m^{-1} at 160°C when doped with 1300–1600 mol% phosphoric acid (Qingfeng et al., 2001).

So, HT-PEMFC based on PBI membrane has excellent properties; therefore, many researchers devoted their efforts to this kind of fuel cell. Ionescu (2016) reported that the impacts of gas channel geometry and cathode gas flow velocity on HT-PEMFC performance in the range from 0.02 m/s up to 0.42 m/s and with a constant anode gas flow velocity. a) The performance enhances when the flow of cathode gas velocity is increased. b) The current density goes down when the channel width widens. c) The current density is directly proportional to the channel height.

It has been investigated that the effect of functioning temperatures, catalyst layers' thickness, and membrane's thickness on the efficiency of HT-PEMFC and concluded that as the temperature raised from 101°C up to 180°C, the performance enhanced (Xia et al., 2018). The performance increased when the catalyst layers' thickness diminished between 100 μm up to 10 μm, the performance increased when thickness of the membrane diminished between 120 μm up to 20 μm. Kumar et al. (2019) investigated the performance of HT-PEMFC and concluded that as the pressure of channels increased from 1 atm up to 5 atm as the performance improved. As the porosity of the gas diffusion layer (GDL) increased from 0.3 up to 0.5 as the performance ameliorated. As the ionic conductivity of the membrane and electric conductivity of the GDL increased, the efficiency increased, and as the channel's width increased, the performance decreased (Yaghoub et al., 2019). Sezgin et al. (2016) investigated the impact of air velocity (cathode gas velocity) on the efficiency of HT-PEMFC and also the effect of changing hydrogen and air velocities at the same time.

Our goal in this paper is to simulate the effects of increasing the multiplicity of electrode membrane assembly (EMA) on: The efficiency, the size of the stack, the consumption of reactants, and the distribution of reactants in the common anode and common cathode channels of parallel flow fields for a stack of single cells, a stack of double cells, a stack of triple cells, and a stack of four cells.

2. MODEL OF SIMULATION

COMSOL Multiphysics software was used to design the model and simulate the HT-PEM fuel cell models with four different parallel flow field cells: a stack of single cells, a stack of double cells, a stack of triple cells, and a stack of four cells. The electrochemistry module and chemical species transport interface were combined together to investigate the HT-PEM fuel cell. The shape of the parallel flow field stack of single cells used for the simulation is displayed in Figure 1(a). The cell consists of seven sub-parts: 1) Cathode gas channel, 2) Cathode gas diffusion layer (C-GDL), 3) Cathode catalyst layer (C-CL), 4) Membrane, 5) Anode catalyst layer (A-CL), 6) Anode gas diffusion layer (A-GDL), 7) Anode gas channel. Figure 1(b) represents the shape of the parallel flow field stack of double cells connected in series, and it is clear that it consists of thirteen sub-parts (but the horizontal stack of double cells consists of fourteen sub-parts). Figure 1(c) represents the shape of the parallel flow field stack of triple cells connected in series, and it is evident it consists of nineteen sub-parts (but the horizontal stack of triple cells consists of twenty-one sub-parts). Figure 1(d) represents the shape of the parallel flow field stack of four cells connected in series, and it is evident it consists of twenty-five sub-parts (but the horizontal stack of four cells consists of twenty-eight sub-parts). The anode channels and common anode channels were supplied with the pure hydrogen, and the cathode channels and common cathode channels were supplied with the air because it is rich with oxygen.

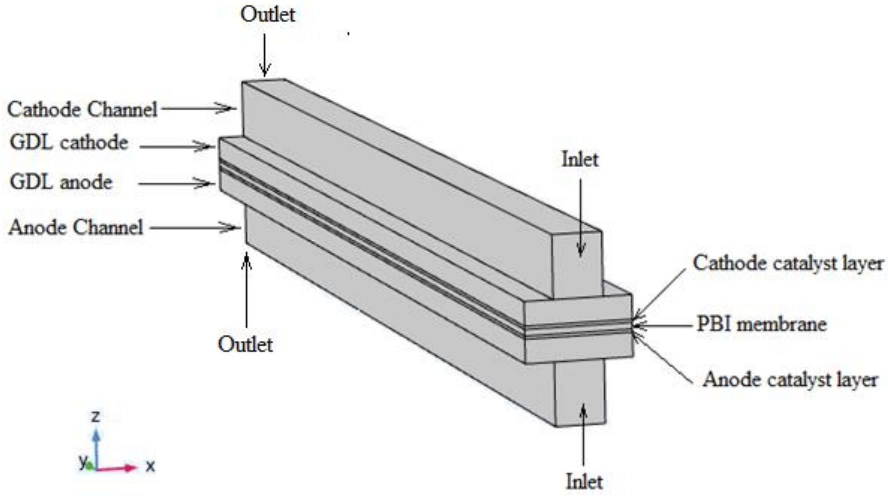

Fig 1. (a) The shape of the parallel flow field of a single-cell stack.

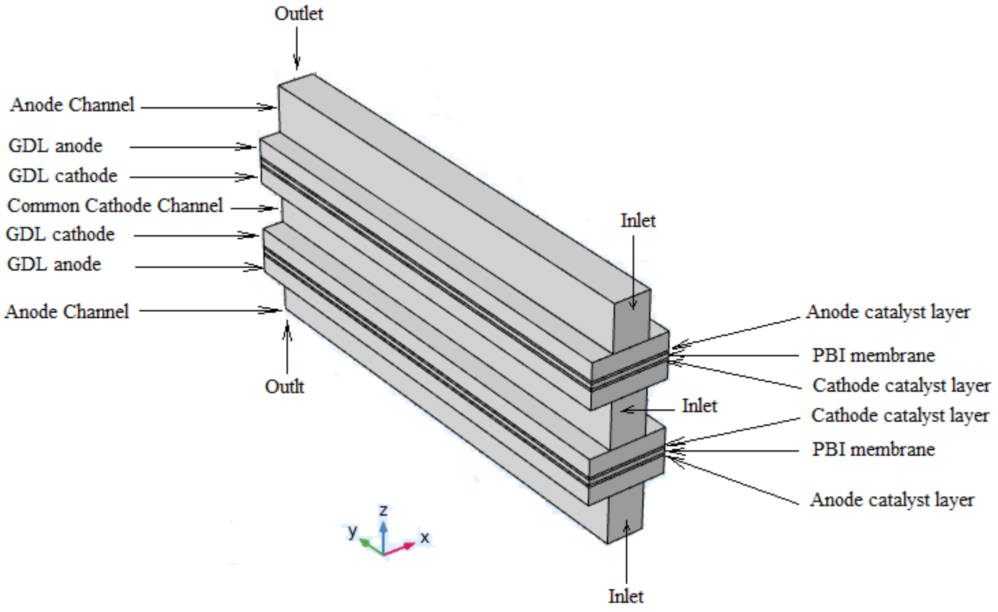

Fig 1. (b) The shape of the parallel flow field of the stack double cell.

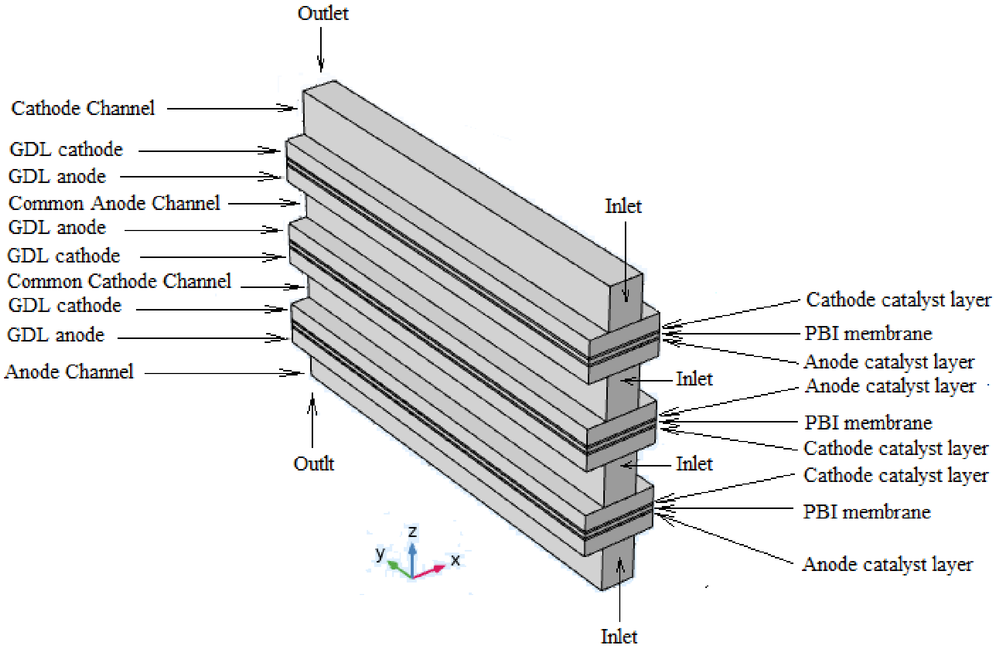

Fig 1. (c) The shape of the parallel flow field of the stack triple cell.

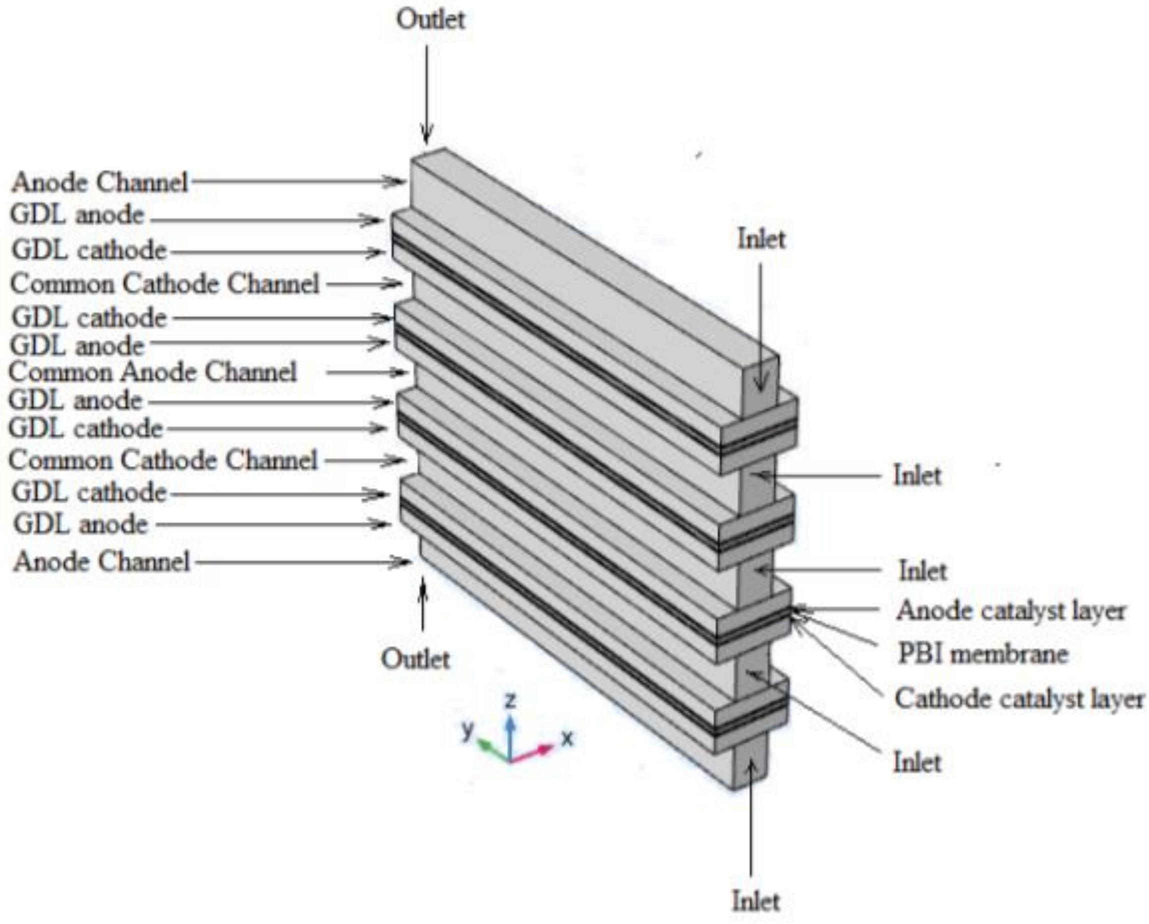

Fig 1. (d) The shape of the parallel flow field of the stack four cell.

3. GENERAL HYPOTHESIS

In this paper we have assumed the following points: A 3D model, single-phase problem, no exchange of water through the PBI membrane (due to the water drag coefficient of PBI being nearly zero) (Weng et al. 1996). A steady-state, isothermal, impermeable membrane for the reactant gases; the flow is treated as laminar because of low gas velocities, and the gas is considered an incompressible and ideal gas.

The chemical reactions of HT-PEMFCs take place in the A-CL and C-CL and are described by the equations (1) and (2), respectively, and then there is a loss of mass at the A-CL and a gain in mass at the C-AL, as shown in the equations (1) and (2).

$$H_2(g) \rightarrow 2H^+_{(s)} + 2e^-, \text{ (at the anode side)} \tag{1}$$

$$½\, O_2(g) + 2H^+(s) + 2e^- \rightarrow H_2O(g), \text{ (at the cathode side)} \tag{2}$$

As a result of the previous two equations, the total mass is preserved; hence, equation (3) gives the profile of continuity of the mass in HT-PEMFCs (Peng & Lee, 2006).

$$\nabla(\rho u) = s_{\mathrm{m}} \tag{3}$$

Where s_{m} is the source term, which is different from zero only in catalyst layers where the chemical reaction is happening.

At the A-CL

$$s_{\mathrm{m}} = -\frac{M_{\mathrm{H_2}}}{2F} j_{\mathrm{a}} \tag{4}$$

At the C-CL

$$s_{\mathrm{m}} = -\frac{M_{\mathrm{O_2}}}{4F} j_{\mathrm{c}} + \frac{M_{\mathrm{H_2O}}}{2F} j_{\mathrm{c}} \tag{5}$$

And

$$\rho = \sum_{\mathrm{i}} (x_{\mathrm{i}} M_{\mathrm{i}}) P/(RT) \tag{6}$$

And ρ denotes the density of the gas mixture, u is the gas mixture velocity vector in (m/s), M_{i} is the molar mass of the type i, R is the universal gas constant, T is temperature in (K), x_{i} is the molar fraction of the type i, F is Faraday's constant, and j_{a}, j_{c} are the transfer current density of the anode and cathode catalyst layers, respectively.

Navier–Stokes Eq. (7) governs the momentum in the flow gas channels (Qingfeng et al., 2001).

$$-\nabla P + \nabla\left[\mu(\nabla u + (\nabla u)^{\mathrm{T}}) - \frac{2}{3}\mu(\nabla u)\right] + f = \rho(u\nabla)u \tag{7}$$

And ∇ is the Laplace operator, P is the pressure (N/m^2), μ is the dynamic viscosity, and f denotes the force term (kg/m^2s^2) including the influence of gravity and volume forces.

Brinkman-Darcy Eq. (8) governs the momentum in porous media such as A-GDL, A-CL, C-GDL, and C-CL (Kumar et al., 2019).

$$\nabla[-P\,I + \frac{\mu}{\varepsilon}(\nabla v + (\nabla v)^{\mathrm{T}}) - \frac{2\,\mu}{3\,\varepsilon}(\nabla v)\,I] - (\frac{\mu}{k} + \beta_{\mathrm{F}}|v| + \frac{S_m}{\varepsilon^2})v + f = \frac{\rho}{\varepsilon}(v\,\nabla)\frac{v}{\varepsilon} \tag{8}$$

Where ε is the porosity of the porous medium, v is the fluid velocity in the porous medium, and k is the effective permeability of the porous medium, I is the unity matrix of the order 3 × 3, S_{m} is the mass source (or the source term) $(\mathrm{kg/m^3\ s})$ and it is given by the equations (4) and (5), and β_{F} is the Forchheimer drag coefficient$(\mathrm{kg/m^4})$.

Stefan–Maxwell Eq. (9) describes the types of gas conservation (Ubong et al., 2009).

$$\nabla\left[-\rho\omega_{\mathrm{i}} \sum_{j=1}^{\mathrm{N}} D_{\mathrm{ij}}^{eff}\left(\frac{M}{M_{\mathrm{j}}}\left(\nabla\omega_{\mathrm{j}} + \omega_{\mathrm{j}}\frac{\nabla M}{M}\right) + \left(x_{\mathrm{j}} - \omega_{\mathrm{j}}\right)\frac{\nabla P}{P}\right) + \omega_{\mathrm{i}}\rho u\right] = R_{\mathrm{i}} \tag{9}$$

Where ω is the mass fraction, $D_{\mathrm{ij}}^{\mathrm{eff}}$ is the effective diffusion coefficient, and R_i is the reaction rate of species i and different than zero only in A-CL and C-CL and is given as by:

$$R_{\mathrm{H_2O}} = \frac{|j_{\mathrm{c}}|}{2F} M_{\mathrm{H_2O}} \tag{10}$$

$$R_{\mathrm{O_2}} = -\frac{|j_{\mathrm{c}}|}{4F} M_{\mathrm{O_2}} \tag{11}$$

$$R_{\mathrm{H_2}} = -\frac{j_{\mathrm{a}}}{2F} M_{\mathrm{H_2}} \tag{12}$$

$$D_{\mathrm{ij}}^{\mathrm{eff}} = D_{\mathrm{ij}} \varepsilon^{1.5} \tag{13}$$

Where D_{ij} is the binary diffusion coefficient and will be described hereafter, and j_{a} and $j_{\mathrm{c}}$are obtained from the simplified Butler–Volmer equation, which is given as

$$j_{\mathrm{a}} = a i_{0,\mathrm{a}}^{\mathrm{ref}} (\frac{C_{\mathrm{H_2}}}{C_{\mathrm{H_2,ref}}})^{0.5} (\frac{\alpha_{\mathrm{a}} + \alpha_{\mathrm{c}}}{RT} F \eta_{\mathrm{a}}) \tag{14}$$

$$j_{\mathrm{c}} = a i_{0,\mathrm{c}}^{\mathrm{ref}} (\frac{C_{\mathrm{O_2}}}{C_{\mathrm{O_2,ref}}}) (-\frac{\alpha_{\mathrm{c}}}{RT} F \eta_{\mathrm{c}}) \tag{15}$$

In addition, η_{a} and η_{c} are the overpotentials of the anode and cathode, respectively, and are calculated as follows:

$$\begin{cases} \eta_{\mathrm{a}} = \phi_{\mathrm{s}} - \phi_{\mathrm{e}} \\ \eta_{\mathrm{c}} = \phi_{\mathrm{s}} - \phi_{\mathrm{e}} - U_{\mathrm{OC}} \end{cases} \tag{16}$$

Where U_{OC} is the open circuit voltage, C_{i} is the concentration of gas of the type i, $C_{\mathrm{i,ref}}$ is the reference molar concentration of gas of the type i. In the anode, α_{a}, α_{c} of the eq. (14) are anodic and cathodic transfer coefficients for the hydrogen oxidation reaction. In the cathode, α_{c} of the eq. (15) is the cathodic transfer coefficient for the oxygen reduction reaction.

$i_{0,\mathrm{a}}^{\mathrm{ref}}$ and $i_{0,\mathrm{c}}^{\mathrm{ref}}$ are reference exchange current density at the anode and cathode, respectively. Moreover, the binary diffusion coefficients were calculated using the equations (17), (18), (19) and (20) (Celik et al., 2014).

$$D_{\mathrm{H_2-H_2O}} = 9.15 \times 10^{-5} (\frac{T}{307.1\ \mathrm{K}})^{1.75}\ \mathrm{m^2/s} \tag{17}$$

$$D_{\mathrm{N_2-H_2O}} = 2.56 \times 10^{-5} (\frac{T}{307.15\ \mathrm{K}})^{1.75}\ \mathrm{m^2/s} \tag{18}$$

$$D_{\mathrm{O_2-N_2}} = 2.2 \times 10^{-5} (\frac{T}{293.2\ \mathrm{K}})^{1.75}\ \mathrm{m^2/s} \tag{19}$$

$$D_{\mathrm{O_2-H_2O}} = 2.82 \times 10^{-5} (\frac{T}{308.1\ \mathrm{K}})^{1.75}\ \mathrm{m^2/s} \tag{20}$$

Where the temperature, T in the previous equations should be in Kelvin. The conservation of electric charge has been obtained from the following two equations (21) and (22) (Ubong et al., 2009).

$$\nabla.(-\sigma_{\mathrm{sol}} \nabla \phi_{\mathrm{sol}}) = S_{\mathrm{sol}} \tag{21}$$

$$\nabla.(-\sigma_{\mathrm{mem}} \nabla \phi_{\mathrm{mem}}) = S_{\mathrm{mem}} \tag{22}$$

Here, ϕ is the phase potential, σ_{sol} is the electric conductivity of the solid phase, σ_{mem} is the protonic conductivity of the membrane, S_{sol} is the current source term of the solid phase, and S_{mem} is the current source term of the electrolyte.

For the A-CL:

$$S_{\mathrm{mem}} = j_{\mathrm{a}} \text{ and } S_{\mathrm{sol}} = -j_{\mathrm{a}} \tag{23}$$

For the C-CL:

$$S_{\mathrm{mem}} = j_{\mathrm{c}} \text{ and } S_{\mathrm{sol}} = -j_{\mathrm{c}} \tag{24}$$

All the amounts of variables used in the modeling are listed in Table 1.

4. RESULTS AND DISCUSSION

4.1 Validation of results

Figure 2 shows the contrast of our polarization curve results obtained by simulation of the parallel flow field stack single cell shown in Figure 1(a) with the experimental work of (Sezgin et al. 2016). At 160°C, 1.18 atm, the inlet gas velocities in the anode and cathode, respectively, are: $U_{\mathrm{\_in\_anode}} = 0.2\ \mathrm{m/s}$, $U_{\mathrm{\_in\_cathode}} = 0.5\ \mathrm{m/s}$, and with thicknesses of GDL, CL, and membrane are $550\ \mu\mathrm{m}$, $20\ \mu\mathrm{m}$ and $75\ \mu\mathrm{m}$ respectively, which are in conformity with the experiment parameters. From Figure 2 we can notice that there is an excellent match between our simulation results and the experimental data; this allows us to rely on our model for the comparison between the four systems given in Figure 1(a), (b), (c), and (d) used in this paper.

Table 1. Values of variables used for simulation modeling to examine our model

Parameter	Name	Value
L	Cell length	20 [mm]
*H*_ch	Channel height	0.75 [mm]
*W*_ch	Channel width	75 [mm]
*W*_rib	Rib width	1.5 [mm]
*H*_gdl	GDL thickness	0.55 [mm]
*H*_cl	Porous electrode thickness (CL)	0.02 [mm]
H_mem	Membrane thickness	0.075 [mm]
ε_gdl	GDL porosity	0.5
*K*_gdl	GDL permeability	1.18e-11 [m^2]
σ_{sol}	GDL electric conductivity	687.5 [S/m]
μ_a	Anode viscosity	1.19e-5 [Pa.s]
μ_c	Cathode viscosity	2.46e-5 [Pa.s]
*M*H2	Hydrogen molar mass	0.002 [kg/mol]
*M*N2	Nitrogen molar mass	0.028 [kg/mol]
*M*O2	Oxygen molar mass	0.032 [kg/mol]
*D*_H2_H2O	H2-H2O Binary diffusion coefficient	1.6703e-4 [m^2/s]
*D*_N2_H2O	N2-H2O Binary diffusion coefficient	4.6719e-5 [m^2/s]
*D*_O2_N2	O2-N2 Binary diffusion coefficient	5.1187e-5 [m^2/s]
T	Cell temperature	433.15 [k]
*p*_ref	Reference pressure	120000 [Pa]
*V*_cell	Cell voltage	0.6 [V]
ε_l	Electrolyte phase volume fraction	0.4
ε_cl	Open volume fraction for gas diffusion in porous electrodes	0.42
*K*_cl	Permeability of porous electrode	2.36e-12 [m^2]
σ_{mem}	Membrane conductivity	10 [S/m]
*U*_in_anode	Anode inlet flow velocity	0.2 [m/s]
*U*_in_cathode	Cathode inlet flow velocity	0.5 [m/s]
$C_{\text{O2\_ref}}$	Oxygen reference concentration	40.88 [mol/m^3]
$C_{\text{H2\_ref}}$	Hydrogen reference concentration	40.88 [mol/m^3]
*w*H2O_in	Inlet water mass fraction	0.002
*w*H2_in	Inlet hydrogen mass fraction	0.99
*w*O2_in	Inlet oxygen mass fraction	0.208
R	Universal gas constant	8.314 [J/k mol]
F	Faraday’s constant	96487 [C/mol]

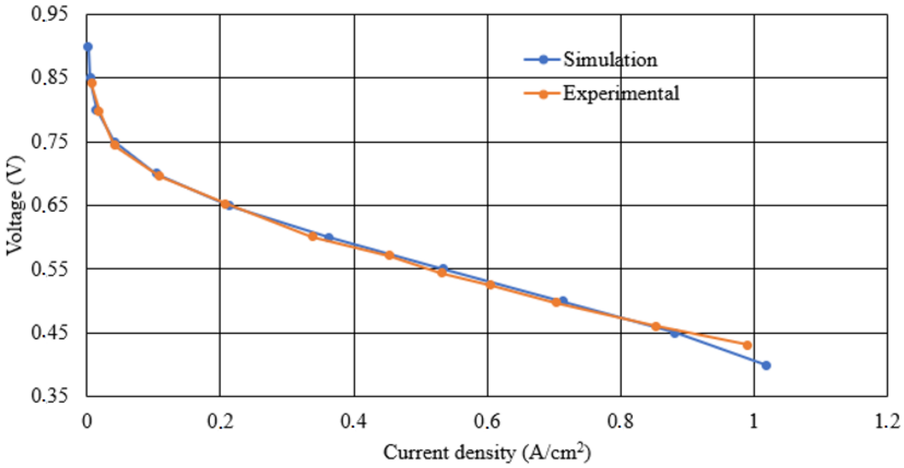

Fig 2. The validation of our polarization curve obtained from simulation using the single cell shown in Figure 1(a) with the experimental test of Sezgin *et* al. (2016).

4.2 Polarization curves

In order to check the performance of the four different stacks, we relied on the comparison of their polarization curves (*V*-*I*). Figure 3 stands for polarization curves of parallel flow field stack of single, double, triple, and four cells. It means we investigated the impact of the pluralism of GDL, CL, and membrane layers on the efficiency of planar parallel fuel cells with the same conditions and same dimensions of GDL, CL, and membrane layers. From Figure 3 we can see that at 0.4 V the current density is 0.94 $\mathrm{A/cm^2}$ for the stack single cell, 1.8 $\mathrm{A/cm^2}$ for the stack double cell, 2.77 $\mathrm{A/cm^2}$ for the stack triple cell, and 3.67 $\mathrm{A/cm^2}$ for the stack four cell. As well as at 0.6 V the current density is 0.34 $\mathrm{A/cm^2}$ for the single cell, 0.68 $\mathrm{A/cm^2}$ for the double cell, 1.03 $\mathrm{A/cm^2}$ for the triple cell, and 1.37 $\mathrm{A/cm^2}$ for the four-cell. It is evident that as the number of electrode membrane assemblies (EMAs) doubles the current density is doubled; as EMAs triple, the current density is tripled; and as EMAs quadruple, the current density is quadrupled. This means as the number of EMAs increases as the performance enhances, we can elucidate this result that the planar cells here are connected in series and without loss of current density.

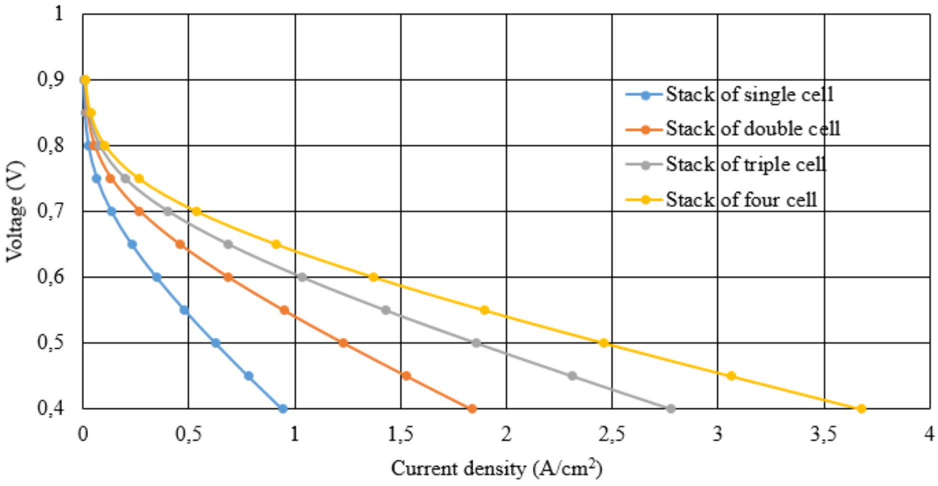

Fig 3. Polarization curves of parallel flow field, stack of single cell, stack of double cell, stack of triple cell, and stack of four cells.

4.3 Anode hydrogen concentration

Figure 4 represents the hydrogen concentration in the anode channels, common anode channel, A-GDLs and common anode GDLs of parallel flow field (a) stack single cell, (b) stack double cell, (c) stack triple cell, and (d) stack four cell at $V_{-\text{cell}} = 0.4$ V. It is obvious that

- The gas channels of a single-cell stack are the anode channel (the lower channel) and the cathode channel (the upper channel).
- The gas channels of a stack double cell are the upper anode channel and lower anode channel and one common cathode channel located between the two anode channels.
- The gas channels of the stack triple cell are the lower anode channel, common anode channel, common cathode channel, and upper cathode channel.
- The gas channels of stack four cells are the upper and lower anode channels, the common anode channel, and two common cathode channels.

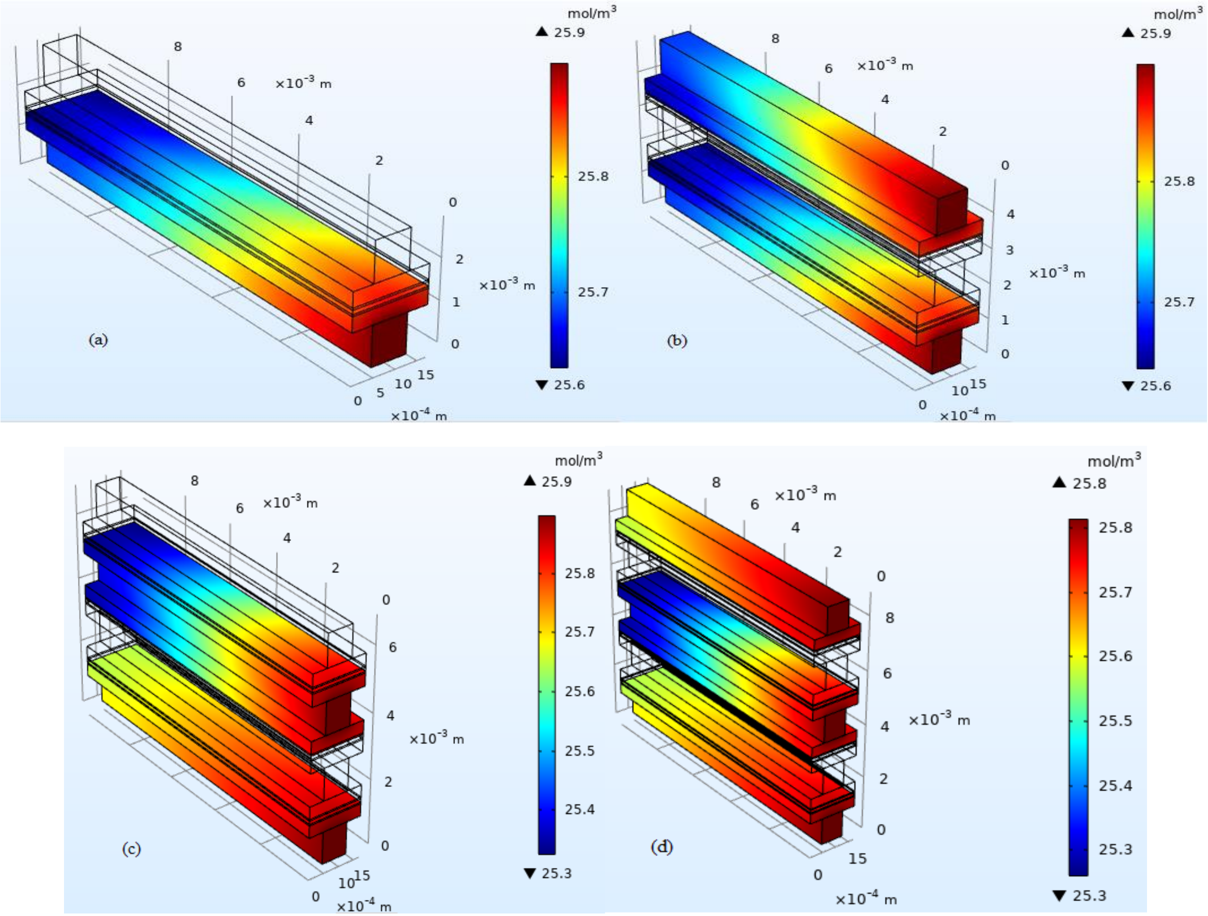

Fig 4. Anode hydrogen concentration of parallel flow field (a) stack single cell (b) stack double cell (c) stack triple cell (d) stack four cell at $V_{-\text{cell}} = 0.4$ V.

Hence, we might highlight three remarks in Figure 4 (a), (b), (c), and (d). The first remark is that as we move along the direction of the flow inside anode channels and common anode channels, as the concentration of hydrogen decreases due to consumption. In the second remark, we can see the fastest decrease in hydrogen concentration in the common anode channels of the stack triple cell and stack four cell because the latter is sandwiched between two EMAs, so the common anode channel here feeds two EMAs simultaneously with hydrogen. That is why it is the fastest decrease in hydrogen concentration. The third remark is that the decrease of hydrogen concentration in the anode channel of the stack single cell in Figure 4(a) is faster than in the upper and lower anode channels of the stack double cell in Figure 4(b). Owing to the single cell in the stack, there is one cathode channel feeding one EMA by oxygen, whereas in the double-cell stack, there is one common cathode channel feeding two EMAs by oxygen. As a consequence, the oxygen concentration in the CLs of the stack double cell will be lower than the oxygen concentration in the CL of the stack single cell, which leads to a faster consumption of hydrogen in the stack single cell than in the stack double cell.

4.4 Cathode oxygen concentration

Figure 5 depicts the oxygen concentration in cathode channels, common cathode channels, C-GDLs, and common cathode GDLs of parallel flow field (a) stack single cell (b), stack double cell, (c) stack triple cell, and (d) stack four cell at $V_{-\text{cell}} = 0.4$ V. Likewise, here we noticed three notes: as we move towards the direction of the flow inside cathode channels and common cathode channels, the oxygen concentration decreases due to its consumption at the CLs to produce water, heat, and electricity. In the second note, we can see the fastest decrease in oxygen concentration in the common cathode channel and common cathode GDLs of the stack double, triple cells, and four cells; see Figure 5(b), (c), and (d). Because each of them is feeding two EMAs with oxygen at the same time. The last note is that the decreasing of oxygen concentration in the cathode channel and C-GDL of the stack single cell is faster than in the cathode channel and C-GDL of the stack triple cell. Due to the EMA of the cathode channel in the stack, a single cell is getting the hydrogen from the anode channel, and the adjacent EMA of the cathode channel in the triple cell is getting the hydrogen from the common anode channel. As a result, the quantity of hydrogen diffused in the EMA of a single cell will be higher than the quantity of hydrogen diffused in the adjacent EMA of the cathode channel in the triple cell.

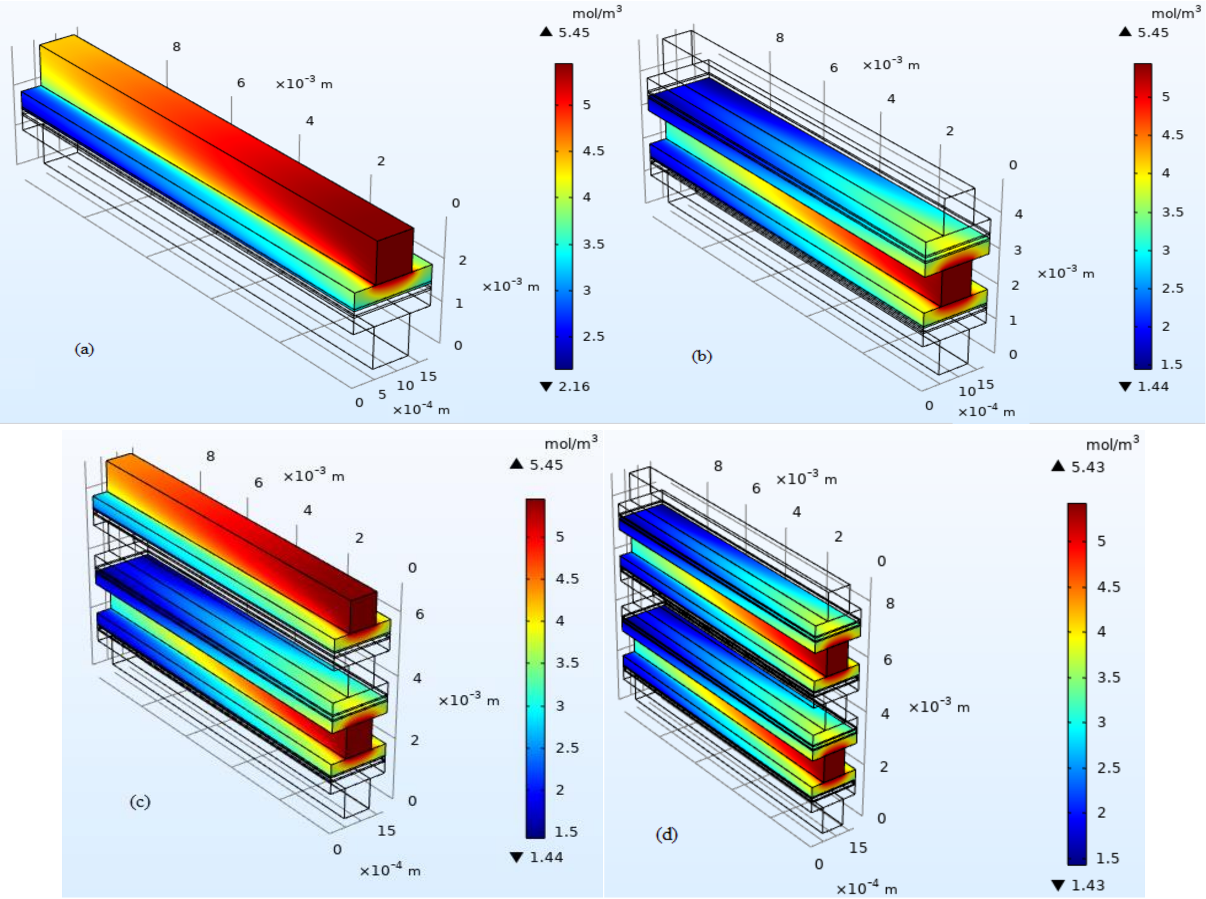

Fig 5. Cathode oxygen concentration of parallel flow field (a) single cell (b) double cell (c) triple cell (d) four cell at $V_{-\text{cell}} = 0.4$ V.

4.5 Cathode water concentration

Figure 6 shows the water concentration in the cathode channels, common cathode channels, C-GDLs, and common cathode GDLs of parallel flow field (a) stack single cell (b) stack double cell (c) stack triple cell and (d) stack four cells at $V_{-\text{cell}} = 0.4$ V. As well as here, we have three comments. The first one is as we move towards the direction of the flow inside cathode channels, common cathode channels, C-GDLs, and common cathode GDLs, the water concentration increased due to the production of water as well as the traffic jam of the produced water. In the second comment, we can see the fastest increase in water concentration appeared in common cathode channels of stack double, triple, and four cells, because the common cathode channels are getting water from the upper EMA and the lower EMA at the same time. The last comment notes that the water concentration in C-GDL of the single-cell stack increased faster than in C-GDL of the triple-cell stack. Because the anode channel in the single cell is feeding only one MEA with hydrogen, whereas the common anode channel in the triple cell is feeding two MEAs with hydrogen, more protons will be abundant in the MEA of the single cell. Leading to water concentration in C-GDL of a single cell being higher than the water concentration in C-GDL of a triple cell.

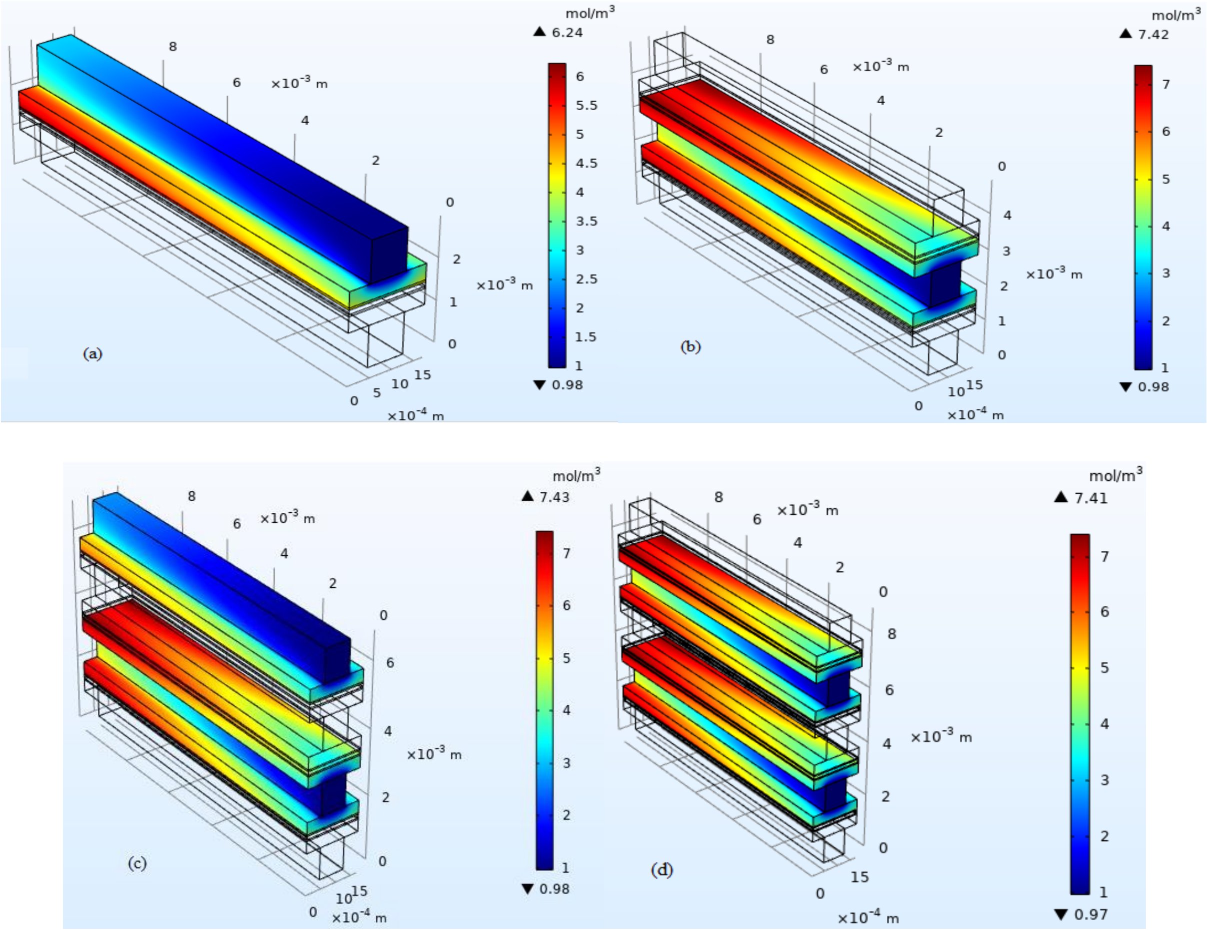

Fig 6. Cathode water concentration of parallel flow field (a) single cell (b) double cell (c) triple cell (d) four cell at $V_{-\text{cell}} = 0.4$ V.

5. CONCLUSION

The vertical architecture and the fast consumption of reactants in the common anode and cathode channels are the novelties of this paper. However, a 3D, isothermal, steady-state, uncompressible gas, ideal gas, impermeable membrane for the reactant gases and water, a single-phase model, and a new architecture are used to build stack doubles, triples, and four cells, which are adopted in this work. The results of our simulation are compared with experiment results. An excellent match is obtained and is shown in Figure 2. The new geometry of stack double, triple, and four cells created the common anode channels and common cathode channels that can feeds two EMAs with reactants simultaneously. This idea can reduce the volume of the whole stack and gives an excellent distribution of reactants in the common channels because each common channel can feed two EMAs at the same time. The most important result is that when the cell is doubled, the performance is doubled; when the cell is tripled, the performance is tripled; and when the cell is quadrupled, the performance is quadrupled, which means we could connect the cells in series. This architecture leads to reducing the length of channels because the inlet reactant gases of the common channels will be consumed faster than in the single cell. Also in this paper, we managed to reduce the number of components of the stack double cell from fourteen sub-parts to thirteen sub-parts. The number of components of the stack triple cell goes from twenty-one sub-parts to nineteen sub-parts, and the number of components of the stack four cell goes from twenty-eight sub-parts to twenty-five sub-parts; as a result, the total volume of the stack is reduced either in the stack double, triple, or four cells.

As a comparison of the outcome of our work with the results of the work of Mohammadi-Ahmar et al. (2016). We can conclude that we obtained the same results as we increased the number of EME as the performance improved, but our work is much better because the parallel flow stack cells are more feasible and applicable in the laboratory than the circular flow cells of Mohammadi-AhmarB et al. (2016).

ACKNOWLEDGEMENTS

A many thanks to the Faculty of Process Engineering, University of Constantine 3, Saleh Boubnider, Algeria, for allowing me to use their licensed COMSOL to perform this work.

REFERENCES

Caglayan, D. G., Sezgin, B., Devrim, Y., Eroglu, I. (2018). Three-dimensional non-isothermal model development of high temperature PEM Fuel Cells. International Journal of Hydrogen Energy 2018 ; 43(23) : 10834-8. doi:org/10.1016/j.ijhydene.2018.01.176.

Çelik, M., Özisik, G., Genç, G., Yapici, H. (2014). The effect of microporous layer in phosphoric acid doped Polybenzimidazole polymer electrolyte membrane fuel cell. J Appl Mech Eng, 3(1): 1000133-6. doi.org/10.4172/2168-9873.1000133.

Cheddie, Denver, F., Munroe, Norman D.H. (2006). Three-dimensional modeling of high temperature PEM fuel cells. Journal of Power Sources 2006; 160: 215-9. doi:org/10.1016/j.jpowsour.2006.01.035.

Ionescu, V. (2016). Simulating the effect of gas channel geometry on PEM fuel cell performance by finite element method. Procedia Technology 2016; 22: 713-7. doi.org/10.1016/j.protcy.2016.01.147.

Kumar, J., Devi, J., Bhutto, G.M., Parveen, S., Shafiq, M. (2019). Analysis of spatially modelled high temperature polymer electrolyte membrane fuel cell under dynamic load conditions. Intern Jo Adva Computer Sci Appl 2019; 10(6): 121-10. doi:org/10.14569/IJACSA.2019.0100618.

Mohammadi-Ahmar, A., Osanloo, B., Solati, A., Ghasemi, J. (2016). Performance improvement of the circular PEMFC by using different architectures and number of layers. Energy Convers Manag 2016; 128: 238-12. doi:org/10.1016/j.enconman.2016.09.074.

Peng, J., Lee, S.J. (2006). Numerical simulation of proton exchange membrane fuel cells at high operating temperature. Journal of Power Sources 2006; 162: 1182-10. doi:org/10.1016/j.jpowsour.2006.08.001.

Qingfeng Li, He R., Gao J.-A., Jensen J.O., Bjerrum N.J. (2003). The CO poisoning effect in PEMFCs operational at temperatures up to 200°C. J Electrochem Soc 2003; 150(12): 1599-7. doi.org/10.1149/1.1619984.

Qingfeng, L., Hjuler, H. & Bjerrum, N. (2001). Phosphoric acid doped polybenzimidazole membrane physiochemical characterization and fuel cell applications. J Appl Electrochem 2001; 31: 773-7. doi:org/10.1023/A:1017558523354.

Sezgin, B., Caglayan, D.G., Devrim, Y., Steenberg, T., Eroglu, I. (2016). Modeling and sensitivity analysis of high temperature PEM fuel cells by using Comsol Multiphysics. Int J Hydrogen Energy 2016; 41(23): 10001-9. doi:org/10.1016/j.ijhydene.2016.03.142.

Ubong E.U., Shi Z, Wang X. (2009). Three-dimensional modeling and experimental study of a high temperature PBI-based PEM fuel cell. Journal Electrochemical Society B 200; 1276-7. doi.org/10.1149/1.3203309.

Weng, D., Wainright, J.S., Landau, U., Savinell, R.F. (1996). Electro-osmotic drag coefficient of water and methanol in polymer electrolytes at elevated temperatures. Journal Electrochemical Society 1996; 143: 1260-4. doi.org/10.1149/1.1836626.

Wu, H.-W., Kang, D.-Y., Perng, S.-W. (2016). Effect of rectangular ribs in the flow channels of HTPEM fuel cell by a three-dimensional model. Energy Procedia 2016; 105: 1376-6. doi:org/10.1016/j.egypro.2017.03.510.

Xia, L., Zhang, C., Hu, M., Jiang, S., Chin, C.S., Gao, Z., Liao, Q. (2018). Investigation of parameter effects on the performance of high-temperature PEM fuel cell. Int J Hydrogen Energy 2018; 43(52): 23441-8. doi.org/10.1016/j.ijhydene.2018.10.210.

Yaghoub Abdollahzadeh Jamalabadi, M., Ghasemi, M., Alamian, R., Afshari, E., Wongwises, S., Mehdi Rashidi, M., & Safdari Shadloo, M. (2019). A 3D simulation of single-channel high-temperature polymer exchange membrane fuel cell performances. Appl Sci. 9: 3633-17. doi.org/10.3390/app9173633.